nature geoscience

Article

https://doi.org/10.1038/s41561-024-01586-z

Recovery of ecosystem productivity in China due to the Clean Air Action plan

Received: 6 November 2023

Accepted: 15 October 2024

Published online: 15 November 2024

Check for updates

Hao Zhou[1,2,10], Xu Yue[3,10] ✉, Huibin Dai[3], Guannan Geng[4], Wenping Yuan[5], Jiquan Chen[6], Guofeng Shen[7], Tianyi Zhang[8,9], Jun Zhu[3] & Hong Liao[3]

Severe air pollution reduces ecosystem carbon assimilation through the vegetation damaging effects of ozone and by altering the climate through aerosol effects, exacerbating global warming. In response, China implemented the Clean Air Action plan in 2013 to reduce anthropogenic emissions. Here we assess the impact of air pollution reductions due to the Clean Air Action plan on net primary productivity (NPP) in China during the period 2014–2020 using multiple measurements, process-based models and machine learning algorithms. The Clean Air Action plan led to a national NPP increase of 26.3 ± 27.9 TgC yr^{-1}, of which 20.1 ± 10.9 TgC yr^{-1} is attributed to aerosol reductions, driven by both the enhanced light availability as a result of decreased black carbon concentrations and the increased precipitation caused by weakened aerosol climatic effects. The impact of ozone amelioration became more important over time, surpassing the effects of aerosol reduction by 2020, and is expected to drive future NPP recovery. Two machine learning models simulated similar NPP recoveries of 42.8 ± 26.8 TgC yr^{-1} and 43.4 ± 30.1 TgC yr^{-1}. Our study highlights substantial carbon gains from controlling aerosols and surface ozone, underscoring the co-benefits of regulating air pollution for public health and carbon neutrality in China.

China has experienced severe air pollution in recent decades[1]. To improve air quality, the Chinese government implemented a 5 yr Clean Air Action (CAA) plan in 2013[2]. This initiative decreased ambient concentrations of particulate matter smaller than 2.5 μm ($PM_{2.5}$) by approximately 30% in 2017 relative to 2013[2,3], and in turn reduced $PM_{2.5}$-induced deaths by as much as 0.37 million (ref. 4). However, surface ozone (O_3) concentrations increased by 1.9 ppbv yr^{-1} during 2013–2019[5], offsetting the health benefits gained from decreased $PM_{2.5}$ concentrations[6]. In response, a new stage of the CAA plan was developed to reduce both $PM_{2.5}$ and O_3 pollution and initiated in 2018[7].

Although the health benefits of the CAA plan have been explored[3,4], the ecological impacts of air pollution changes have not yet been quantified. The carbon assimilation process in terrestrial ecosystems is sensitive to the radiative effects of aerosols[8] and vegetation damage from O_3 (ref. 9). Aerosols can increase diffuse radiation[10,11] and alter surface meteorology[12,13] (for example, by reducing surface temperature

[1]College of Meteorology and Oceanography, National University of Defense Technology, Changsha, China. [2]Key Laboratory of High Impact Weather (special), China Meteorological Administration, Changsha, China. [3]Jiangsu Key Laboratory of Atmospheric Environment Monitoring and Pollution Control, Jiangsu Collaborative Innovation Center of Atmospheric Environment and Equipment Technology, School of Environmental Science and Engineering, Nanjing University of Information Science & Technology (NUIST), Nanjing, China. [4]State Key Joint Laboratory of Environmental Simulation and Pollution Control, School of Environment, Tsinghua University, Beijing, China. [5]Institute of Carbon Neutrality, Sino-French Institute for Earth System Science, College of Urban and Environmental Sciences, Peking University, Beijing, China. [6]Center for Global Change and Earth Observations, Michigan State University, East Lansing, MI, USA. [7]Laboratory for Earth Surface Processes, College of Urban and Environmental Sciences, Peking University, Beijing, China. [8]State Key Laboratory of Atmospheric Boundary Layer Physics and Atmospheric Chemistry, Institute of Atmospheric Physics, Chinese Academy of Sciences, Beijing, China. [9]Collaborative Innovation Center on Forecast and Evaluation of Meteorological Disasters, NUIST, Nanjing, China. [10]These authors contributed equally: Hao Zhou, Xu Yue. ✉e-mail: yuexu@nuist.edu.cn

https://doi.org/10.1038/s41561-024-01586-z

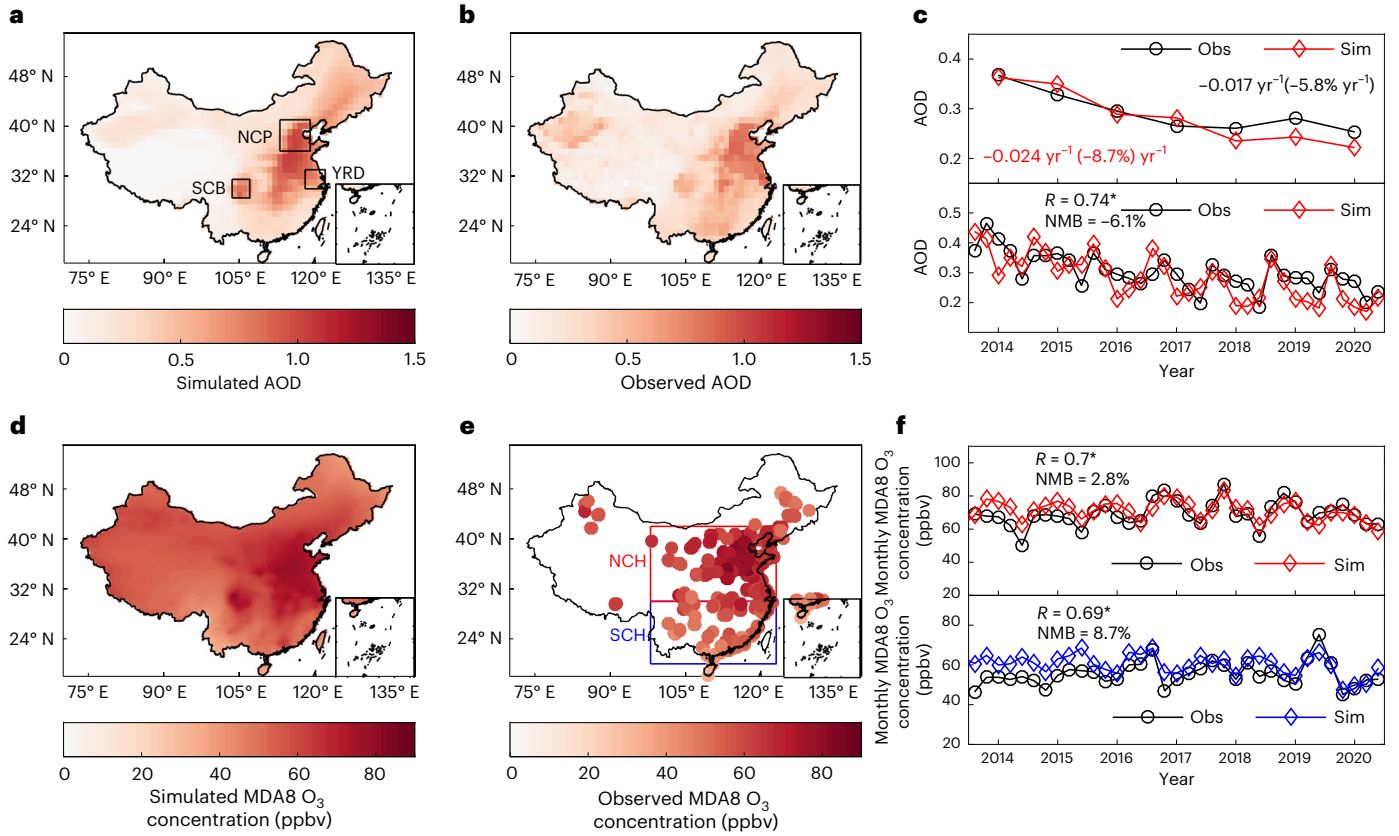

Fig. 1 | Evaluation of the AOD and O_3 concentrations in China for May–September. a,**b**, Spatial patterns of simulated (**a**) and observed (**b**; satellite-based observations) AOD. **c**, Annual mean (top) and monthly mean (bottom) AOD simulated with the Column Radiative Model with aerosol concentrations from GEOS-Chem (Sim) versus observed AOD (Obs) for 2014–2020. Top: annual mean with the trends indicated in the plot. Bottom: monthly mean. **d**,**e**, Spatial patterns of the simulated (**d**) and observed (**e**; ground-based observations) maximum daily 8 h average (MDA8) O_3. **f**, MDA8 O_3 simulated by GEOS-Chem versus observed MDA8 O_3 for 2014–2020 in two regions that show different seasonal variations: North China (top) and South China (bottom) (coloured boxes in **e**). The correlation coefficients (*R*) and normalized mean biases (NMB) between the simulations and observations are listed in **c** and **f**. *Statistically significant *R* value at the 0.01 level. Black rectangles in **a** identify the three key regions with severe air pollution: the North China Plain (NCP, 36–41° N, 113–119° E), the Yangtze River Delta (YRD, 30–33° N, 118–122° E) and the Sichuan Basin (SCB, 28.5–31.5° N, 103.5–107° E). Basemaps (including inset maps) of China are adopted from the Resource and Environment Science and Data Center, ref. 38.

and inhibiting precipitation), both of which then influence the photosynthetic rate of plants. The net effect of these processes depends on the aerosol species[8,14] and environmental conditions[15,16]. Scattering aerosols (such as sulfate and nitrate) can promote photosynthesis by enhancing diffuse radiation, but absorbing aerosols (such as black carbon, BC) inhibit photosynthesis by dampening both direct and diffuse radiation[8]. Clouds substantially reduce direct radiation, thus limiting the diffuse fertilization effects of aerosols[17]. Meanwhile, aerosol cooling effects always increase photosynthesis when the background temperature is higher than optimal temperatures (in tropical regions[12], for example) and aerosol-induced decreases in precipitation inhibit plant photosynthesis through soil water losses[18]. In contrast to the varying effects of aerosols, O_3 consistently reduces plant photosynthesis by affecting stomatal uptake due to its strong oxidizing capacity[19], leading to a net primary productivity (NPP) loss of 14% compared with situations without O_3damage effects in China[18]. Considering that the land ecosystem of China acts as an important carbon sink[20,21], it is critical to explore whether the improvements in air quality due to the CAA plan (CAA-induced) can assist in the recovery of regional carbon assimilation.

Here we explore the overall impacts of CAA-induced changes in aerosols and O_3 on growing-season (May–September) NPP in China during 2014–2020 using two independent approaches. First, a combination of three process-based models is used to isolate the effects of CAA-induced changes in air pollutants on NPP through both radiative and climatic perturbations. This analysis includes the direct and indirect effects of aerosols, as well as vegetation damage from O_3 (Methods). We use the newly developed interactive Model of Air Pollution and Land Ecosystems (iMAPLE)[22] to quantify the changes in ecosystem

Table 1 | Summary of NPP changes caused by aerosols and O_3 during 2014–2020

Influences	Factors	Process-based models	Machine learning models	
		iMAPLE	XGB	RF
ΔNPP due to baseline air pollutants (TgC yr^{-1})	Aerosol RE	27.9±11.7[a]		
	Aerosol CE	−139±17.7		
	O_3 damage	−376±22.6		
	Aerosol+O_3	−487.1±21.7		
ΔNPP due to CAA-induced air pollution changes (TgC yr^{-1})	Aerosol RE	6.2±3.2		
	Aerosol CE	13.9±8.3		
	O_3 damage	6.2±17.6		
	Aerosol+O_3	26.3±27.9	42.8±26.8	43.4±30.1
ΔNPP due to LCC (TgC yr^{-1})	LCC	16.1±8.7	23.4±9	19.5±12.3

ΔNPP, changes in NPP; CE, climatic effects; LCC, land-cover change; RE, radiative effects; RF, random forest algorithm; XGB, extreme gradient boosting algorithm. [a]The values are presented as mean±s.d. for the annual values for 2014–2020.

https://doi.org/10.1038/s41561-024-01586-z

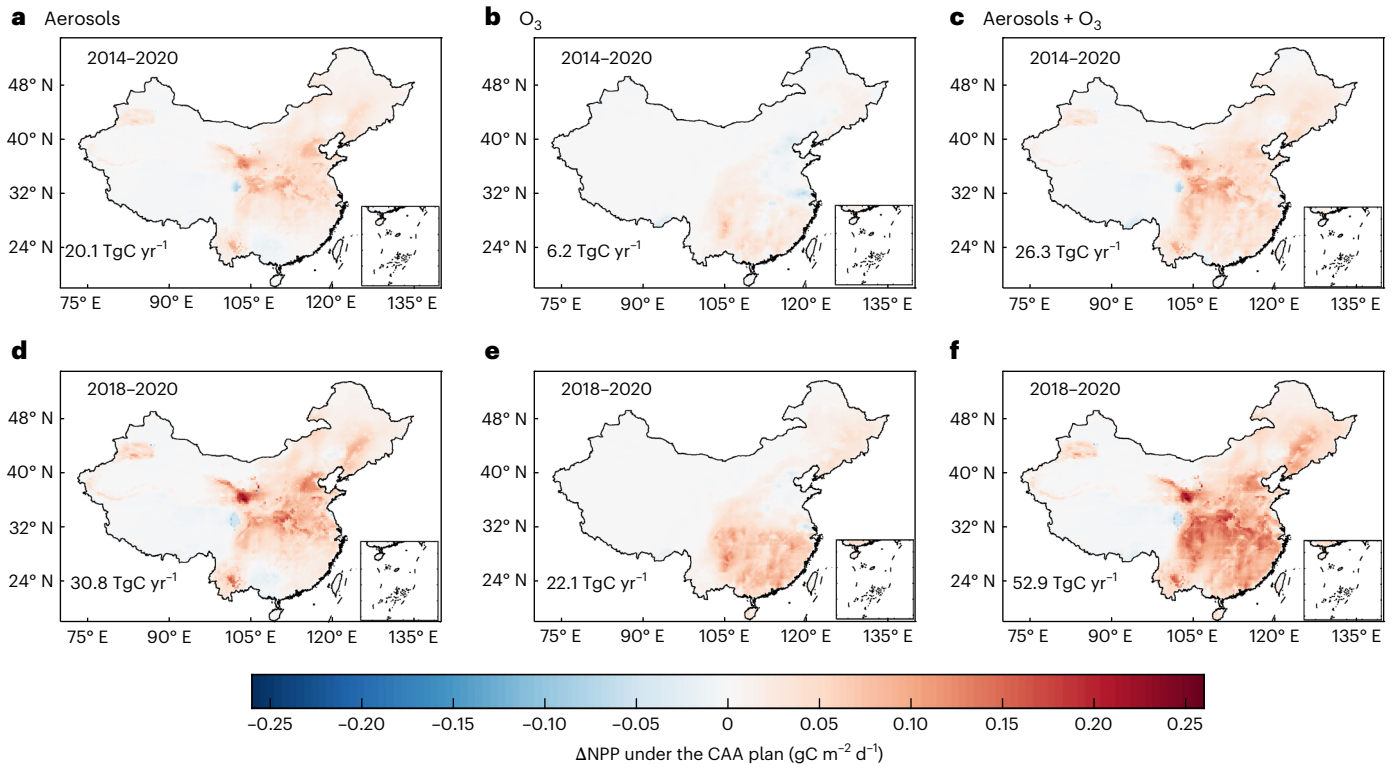

Fig. 2 | NPP recovery following the changes in aerosols and O_3 due to the CAA plan. a–f, ΔNPP during May–September caused by the changes in aerosols (**a**,**d**), surface O_3 (**b**,**e**) and their combined effects (**c**,**f**) between process-based simulations with and without the CAA plan, averaged over 2014–2020 (**a**–**c**) and 2018–2020 (**d**–**f**). The impacts of aerosols on NPP include radiative (changes in diffuse and direct radiation) and climatic (changes in temperature and precipitation) effects. The total changes in national NPP are shown in each panel. Basemaps (including inset maps) of China are adopted from the Resource and Environment Science and Data Center, ref. 38.

NPP resulting from aerosol and O_3 changes due to enforcement of the CAA plan. iMAPLE incorporates a well-validated O_3 stomatal damage scheme[23] and a two-leaf canopy radiative scheme[24], the latter of which helps to differentiate photosynthetic responses to the changes in diffuse and direct radiation caused by aerosols[25] (Methods). Two machine learning models are then applied independently to further resolve the impacts of CAA-induced changes in air pollutants on regional NPP, serving as a cross-validation for the process-based models. We aim to quantify the differences in carbon assimilation with and without stringent air pollution regulations, thereby assessing NPP recovery in response to air pollution controls following the establishment of the CAA plan.

Changes in air pollutants and the contributions of the CAA plan

During 2014–2020, high aerosol optical depths (AOD > 0.5) were observed in eastern China, especially over the North China Plain (NCP) and the Sichuan Basin (SCB), due to high anthropogenic emissions (Fig. 1b). The national AOD showed a decreasing trend of −0.017 yr^{-1} (−5.8% yr^{-1}) during this period (Fig. 1c). Driven by reduced anthropogenic emissions (Supplementary Fig. 1), the chemical transport model (GEOS-Chem; Methods) reproduced the spatial pattern of the observed AOD (Fig. 1a) with a comparable trend (Fig. 1c). Regionally, the hotspots over the NCP and SCB showed the steepest decreasing trends of up to −0.05 yr^{-1} (Supplementary Fig. 2). Similarly, high O_3 concentrations were observed on the NCP, with secondary centres in the Yangtze River Delta (YRD) and the SCB (Fig. 1e). The simulated O_3 from GEOS-Chem matched the observed pattern (Fig. 1d) with high correlations (r) and low biases (b) in northern (r = 0.7 and b = 2.8%) and southern (r = 0.69 and b = 8.7%) China (Fig. 1f).

Compared with the simulation with anthropogenic emissions fixed to 2013 levels, the simulated AOD with the CAA in place showed mean reductions of −0.05 yr^{-1} during 2014–2020, with regional hotspots showing mean reductions over −0.5 yr^{-1} in the NCP and SCB after 2018 (Supplementary Fig. 3). This leads to a large decreasing trend of −0.014 yr^{-2} (Supplementary Fig. 4), which accounts for over 58% of the total AOD trend over the same period (Fig. 1c). For aerosol species, the AOD of sulfate/nitrate and BC aerosols decreased continuously, but organic carbon (OC) aerosols showed positive AOD changes in 2013–2015 (Supplementary Fig. 5), probably due to increased anthropogenic emissions of non-methane volatile organic compounds (VOCs) (Supplementary Fig. 1) and decreases in the hygroscopicity of OC owing to lower concentrations of sulfate aerosols[26].

With the implementation of the CAA plan, surface O_3 showed an increase of 0.76 ppbv yr^{-1} in 2014–2017 but a decrease of −1.3 ppbv yr^{-1} in 2018–2020 (Supplementary Fig. 4d). Regionally, the CAA plan increased O_3 by 1.77 ppbv yr^{-1} in the NCP, 2.75 ppbv yr^{-1} in the YRD and 0.1 ppbv yr^{-1} in the SCB during 2014–2017 (Supplementary Fig. 6). These changes might have been related to O_3 increases caused by greater concentrations of hydroperoxyl (HO_2) and NO_x radicals following the decreases in $PM_{2.5}$, especially in NO_x-sensitive regions[27], and limited regulation of non-methane VOC emissions in VOC-sensitive regions[28]. The positive change in O_3 shifted to negative in 2018 (Supplementary Fig. 6), when the O_3 reductions in southern China outweighed increases in the NCP. Thereafter, the CAA plan continued to amplify O_3 reductions, which reached −1.68 ppbv in 2019 and −1.88 ppbv in 2020.

NPP recovery under CAA-induced changes in air pollutants

During 2014–2020, baseline air pollution inhibited national NPP by up to −487.1 ± 21.7 TgC yr^{-1} (mean ± s.d.), accounting for −13.6 ± 0.61% of the total NPP in China (Supplementary Section 1). This NPP loss was

https://doi.org/10.1038/s41561-024-01586-z

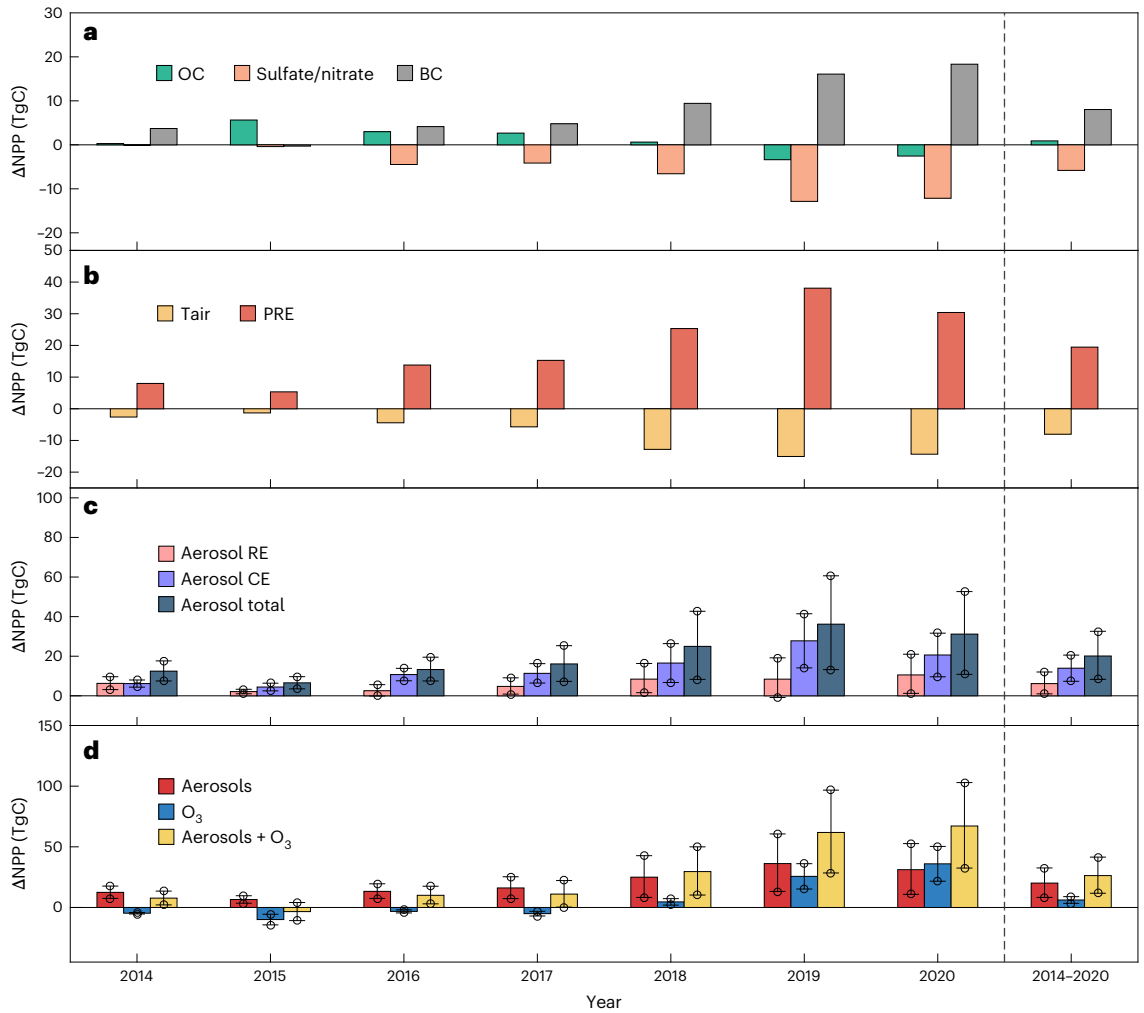

Fig. 3 | The year-to-year NPP recovery attributable to CAA-induced changes in aerosols and surface O_3 in China. a–**c**, Changes in NPP caused by the radiative effects (RE) of different aerosol species (**a**), the climatic effects (CE) of aerosols through varied meteorological perturbations (**b**) and their combined effects (**c**). **d**, The overall aerosol effect is compared with O_3 damage for simulations with and without the CAA plan. The RE of aerosols, calculated using the Column Radiative Model, are decomposed into OC, sulfate/nitrate and BC aerosols. The CE of aerosols are estimated using the mean climatic perturbations simulated by two Earth system models (Methods) and is separated into air temperature (Tair) and precipitation (PRE) effects. The uncertainty ranges for RE in **c** are shown by the error bars ($n = 2$) and the open circles reflect aerosol RE caused by 0.8–1.2 times the simulated aerosol loading. The error bars ($n = 2$) for CE in **c** indicate the variability of NPP responses due to differing climate sensitivities between the two Earth system models (open circles). The error bars ($n = 2$) for O_3 effects in **d** indicate the range of NPP changes due to differing O_3 damage sensitivities (low to high) (open circles).

composed of −111 ± 17.8 TgC yr^{-1} (−3.1 ± 0.5% yr^{-1}) due to aerosols and −376 ± 22.6 TgC yr^{-1} (−10.5 ± 0.6% yr^{-1}) due to O_3 (Table 1 and Extended Data Figs. 1–3). Compared with NPP simulations using anthropogenic emissions fixed to 2013 levels, CAA-induced reductions in aerosols led to an NPP recovery of 20.1 ± 10.9 TgC yr^{-1} during 2014–2020 (Fig. 2a). This recovery comprised 6.2 ± 3.2 TgC yr^{-1} from aerosol radiative effects and 13.9 ± 8.3 TgC yr^{-1} from the effects of aerosols (aerosol climatic effects) (Table 1 and Extended Data Fig. 4). The radiative effects primarily enhanced NPP in southern China through the increased light availability as a result of reduced BC concentrations (Fig. 3a and Extended Data Fig. 5a) outweighing the negative impacts from decreased sulfate and nitrate aerosols (Fig. 3a and Extended Data Fig. 5c). Meanwhile, CAA-induced aerosol reductions promoted NPP in China by increasing precipitation (and thereby water availability; Fig. 3b and Extended Data Fig. 5e), although the associated warming due to aerosol removal dampened NPP over southern China in particular (Fig. 3b and Extended Data Fig. 5d). During 2018–2020, a more pronounced NPP recovery due to reduced aerosols was observed, reaching up to 30.8 ± 5.6 TgC yr^{-1} (9.1 ± 1.2 TgC yr^{-1} from radiative effects and 21.6 ± 5.7 TgC yr^{-1} from climatic effects); this was approximately 2.5 times the NPP recovery found for 2014–2017 (Figs. 2d and 3c), reflecting the benefits of stricter aerosol controls.

The implementation of the CAA plan led to a modest NPP recovery of 6.2 ± 17.6 TgC yr^{-1} in China during 2014–2020 due to the improved O_3 pollution levels (Fig. 2b). This recovery reflected a shift from exacerbated NPP losses of −5.8 ± 2.9 TgC yr^{-1} in 2014–2017 to a notable improvement of 22.1 ± 16 TgC yr^{-1} in 2018–2020 (Fig. 3c). These gains in NPP were primarily observed in southern China. Conversely, the NCP and YRD experienced adverse NPP responses associated with rising O_3 levels (Supplementary Fig. 6). Overall, both aerosols and O_3 contributed to a combined NPP increase of up to 26.3 ± 27.9 TgC yr^{-1} during 2014–2020 (Fig. 2c). The beneficial impacts of aerosols were primarily driven by reductions in BC and increases in precipitation following enforcement of the CAA plan (Fig. 3a,b). The positive influence of O_3 increased markedly, with an average rate of 15.7 TgC yr^{-2} in 2018–2020. Consequently, the CAA-induced variations in aerosols and O_3 resulted in an aggregate enhancement of national NPP of 52.9 ± 20.3 TgC yr^{-1} in 2018–2020 (Fig. 2f), comprising 30.8 ± 5.6 TgC yr^{-1} from aerosols (Fig. 2d) and 22.1 ± 16 TgC yr^{-1} from O_3 (Fig. 2e). Together, these changes offset 10.9% of the contemporary NPP reduction induced by air pollution.

https://doi.org/10.1038/s41561-024-01586-z

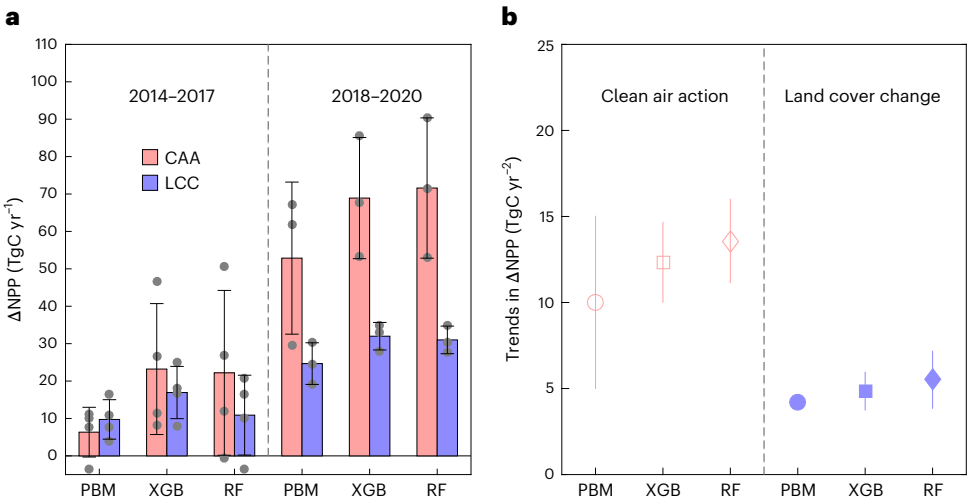

Fig. 4 | NPP changes and trends in China due to the CAA plan and LCC. **a**, ΔNPP over two periods (2014–2017 (left) and 2018–2020 (right)) (**a**) and the corresponding trends in national NPP recovery (2013–2020) (**b**) due to the CAA-induced air pollution changes (red) and LCC (blue). These results are estimated using two machine learning approaches, XGB and RF, and the combination of three process-based models (PBM). The error bars in **a** indicate 1 s.d. of year-to-year NPP changes (grey dots indicate annual values including $n = 4$ for 2014–2017 and $n = 3$ for 2018–2020) and those in **b** represent the 95% confidence intervals ($n = 2$).

Comparisons with NPP recovery from machine learning methods

We further examined the effects of changes in air pollutants on NPP in China during 2014–2020 using two machine learning methods (Fig. 4). These data-driven models can usually achieve high levels of accuracy because they learn directly from measurement data, capturing intricate patterns and dependencies that might be missed by traditional modelling techniques (Methods). Sensitivity analyses showed that air pollutant reductions contributed to an NPP increase of 42.8 ± 26.8 TgC yr^{-1} with XGB and 43.4 ± 30.1 TgC yr^{-1} with RF (Table 1 and Fig. 4a). Over the period 2014–2017, changes in air pollutants led to an average NPP recovery of 23.2 ± 15.2 TgC yr^{-1} with XGB and 22.2 ± 19.1 TgC yr^{-1} with RF (Fig. 4a). A more pronounced NPP recovery was observed in the subsequent period (2018–2020), with increases reaching 68.9 ± 13.2 TgC yr^{-1} with XGB and 71.6 ± 15.3 TgC yr^{-1} with RF. As a result, the implementation of the CAA plan caused positive and significant ($P < 0.05$) trends in NPP recovery up to 12.3 ± 2.4 TgC yr^{-2} with XGB and 13.6 ± 2.5 TgC yr^{-2} with RF models from 2013 to 2020. These trends are comparable to the 10.0 ± 5.0 TgC yr^{-2} estimated by process-based models (Fig. 4b).

Comparisons with NPP recovery due to LCC

Over the past three decades, China's sustained afforestation efforts have substantially contributed to a marked greening trend[29] and an enhanced carbon sink[30]. We also isolated the impact of LCC on NPP recovery as a comparison with CAA-induced NPP gains over the same periods (Fig. 4). Process-based models showed that the increases in tree cover led to an NPP recovery of up to 16.1 ± 8.7 TgC yr^{-1} in China during 2014–2020, with increments from 9.7 ± 4.6 TgC yr^{-1} in 2014–2017 to 24.7 ± 4.5 TgC yr^{-1} in 2018–2020. As a result, positive trends in NPP recovery reached 4.2 ± 0.4 TgC yr^{-2} over the period 2013–2020. Similarly, machine learning models identified that LCC contributed to NPP recoveries of 23.4 ± 9 TgC yr^{-1} with XGB and 19.5 ± 12.3 TgC yr^{-1} with RF in 2014–2020. This recovery further intensified during 2018–2020, reaching 32 ± 3 TgC yr^{-1} with XGB and 31 ± 3 TgC y^{r-1} with RF. Consequently, positive trends in LCC of 4.8 ± 1.1 TgC yr^{-2} and 5.5 ± 1.7 TgC yr^{-2} were found with the two machine learning methods, respectively. Compared with the CAA-induced NPP recovery, recovery due to LCC showed lower magnitudes and trends when using both process-based and machine learning models, suggesting a more substantial NPP recovery driven by short-term air pollution mitigation measures.

Robustness of the derived NPP recovery

Our study quantified the comprehensive impacts of the CAA plan on ecosystem productivity in China. We discovered that CAA-induced changes in aerosols and O_3 consistently promoted NPP by 26.3 ± 27.9 TgC yr^{-1} during 2014–2020 (Fig. 2), which is predominantly attributed to reduced BC concentrations, increased precipitation and decreased O_3 concentrations (Fig. 5). The robustness of these findings is supported by rigorous validations of air pollutants and ecosystem responses. The simulated changes in O_3 and total AOD reproduced the observed spatiotemporal variations (Fig. 1). The simulated AOD of BC showed a decreasing trend of −6.77% yr^{-1} over eastern China, similar to the −7.75% yr^{-1} trend obtained from satellite observations[31] (Supplementary Fig. 7a–c). The simulated surface BC concentrations decreased at a rate of −7.66% yr^{-1}, close to the trend of −9.27% yr^{-1} indicated by a data-fusion model product that combines multi-source observations and emissions inventories[32] (Supplementary Fig. 7d–f). The modelled responses of plant photosynthesis to O_3 were also validated using both global measurements[16] and measurements from China[18] in the literature. Simulated diffuse fertilization effects were evaluated against site-level observations from 167 stations[33] (Supplementary Figs. 8 and 9), and the radiative and climatic effects of aerosols were also validated with other Earth system models[25].

We applied machine learning models to cross-validate the results derived from process-based models. Both machine learning models reported greater NPP recovery than the process-based models on the basis of decadal averages and trends (Fig. 4). The process-based models isolated changes in aerosols and O_3 attributed to CAA-induced controls on anthropogenic emissions, whereas the machine learning models considered the combined effects of anthropogenic and natural emissions and meteorological variations on air pollutants. Despite these discrepancies, previous studies have demonstrated that anthropogenic emissions controls have been the dominant drivers of reductions in air pollutants over recent decades[2,27]. Our analyses using both process-based and machine learning models yielded similar temporal variations and comparable magnitudes of NPP recovery.

Implications and uncertainties

Previous studies have highlighted notable increases in land carbon assimilation in China that were driven by ecological projects such as the Three North Shelterbelt Development Program[34] and the Grain for Green Project[35]. Recent studies have shown that the long-term

https://doi.org/10.1038/s41561-024-01586-z

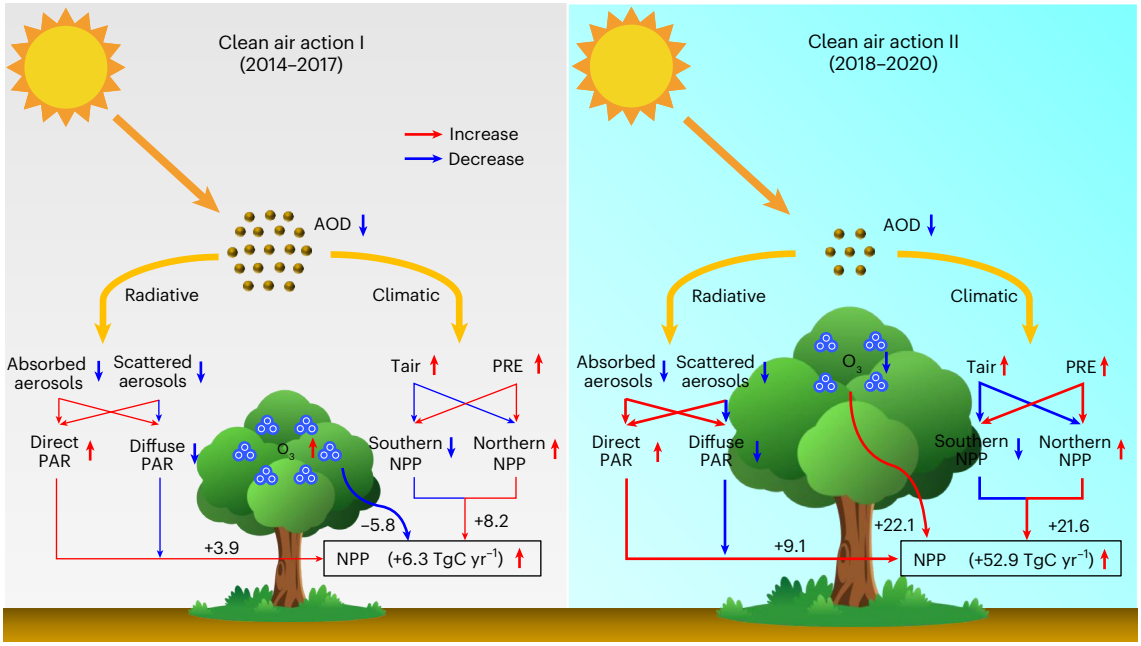

Fig. 5 | NPP responses to aerosol and O_3 changes in different CAA phases. This diagram illustrates various processes related to the effects of aerosols and O_3 on NPP for CAA phase I (2014–2017) (**a**) and CAA phase II (2018–2020) (**b**). Aerosol impacts through both radiative and climatic pathways are shown, along with O_3 damage to NPP in China during 2014–2020. Red lines indicate processes that increase NPP, while blue lines denote processes that decrease NPP. The thicker arrows for 2018–2020 represent stronger NPP changes caused by air pollution mitigation compared with the period of 2014–2017.

afforestation efforts contributed to a recovery of the land carbon sink in China by up to 44% during 1980–2019[30]. By analysing the latest land-cover data for afforestation in China[36], we found that LCC on average accounted for 45–61.2% of NPP recovery attributable to CAA-induced air pollution changes from different methods (Fig. 4a). These results underscore the large benefits of stringent air pollution controls for ecosystem health and regional carbon uptake. Our analyses showed that implementation of the CAA plan boosted NPP recovery more than LCC in China, but their relative impacts on regional carbon sinks remain unclear. This is due to the complex responses of soil respiration, which involve long-term accumulation and slow conversion processes that are not yet fully quantified. Taking soil respiration and other factors into account, we estimated a 25% conversion of the additionally assimilated NPP to the land carbon sink[9]. As a result, the short-term CAA-induced air pollution reduction may have increased the regional carbon sink by 6.6–10.9 TgC yr^{-1}, accounting for 2.5–5.7% of the regional terrestrial sink[20] and 0.25–0.41% of fossil fuel carbon emissions[37] in China.

Our estimates were subject to modelling uncertainties in pollutant concentrations, aerosol climatic effects, linear attributions and O_3 damage sensitivity. To address the uncertainties in aerosol concentrations, we conducted additional sensitivity experiments by applying scaling factors of 0.8 and 1.2 to aerosol loading for specific species. These simulations resulted in NPP enhancements of 2.6 ± 1.4 TgC yr^{-1} and 10.4 ± 5.8 TgC yr^{-1} attributable to aerosol radiative effects, respectively (Fig. 3c), close to the estimate of 6.2 ± 3.2 TgC yr^{-1} obtained under the baseline aerosol loading conditions. For aerosol climatic effects, we conducted two sensitivity experiments to estimate uncertainties from different climate models (Methods), resulting in positive NPP recovery ranging from 9.3 to 18.6 TgC yr^{-1} (Supplementary Fig. 10a,b). Our attribution methods may ignore the nonlinear interactions among different species and climatic variations. The sum of NPP changes, calculated by aggregating the impacts of individual species and aerosol-induced climatic variations (Extended Data Fig. 5), was lower than the results obtained when considering all species and climatic variations together (Fig. 2). Furthermore, there are uncertainties associated with O_3 damage effects in our simulated NPP recovery. To verify the robustness of our results, we used the mean value (6.2 ± 17.6 TgC yr^{-1}) derived from a range of low (4.2 ± 12.7 TgC yr^{-1}) to high (8.1 ± 22.6 TgC yr^{-1}) O_3 damage sensitivities (Fig. 3d).

Despite these uncertainties, we found that a robust NPP recovery of 52.9 ± 20.3 TgC yr^{-1} in 2018–2020 (Fig. 5) could be attributed to the enactment of the CAA plan. Looking ahead, further gains from aerosol removal would be limited because the total NPP damage induced by aerosols was only −111 ± 17.8 TgC yr^{-1}, which is considerably less than the damage of −376 ± 22.6 TgC yr^{-1} induced by O_3 pollution (Extended Data Fig. 1). The second phase of the CAA plan (2018–2020) effectively alleviated O_3 pollution (Supplementary Fig. 6) through the joint control of non-methane VOCs and NO_x (Supplementary Fig. 1). If the current rate of O_3 reduction continues over the next decade, we project a further decrease of ~5.5 ppbv in surface O_3, potentially boosting NPP recovery by 94 TgC yr^{-1} based on 2018–2020 carbon recovery rates. This suggests that there is considerable potential to enhance the land carbon sink through more effective control of surface O_3 in the future[29].

Online content

Any methods, additional references, Nature Portfolio reporting summaries, source data, extended data, supplementary information, acknowledgements, peer review information; details of author contributions and competing interests; and statements of data and code availability are available at https://doi.org/10.1038/s41561-024-01586-z.

References

1. Sheehan, P., Cheng, E., English, A. & Sun, F. China's response to the air pollution shock. *Nat. Clim. Change* **4**, 306–309 (2014).
2. Zheng, B. et al. Trends in China's anthropogenic emissions since 2010 as the consequence of clean air actions. *Atmos. Chem. Phys.* **18**, 14095–14111 (2018).
3. Xue, T. et al. Rapid improvement of PM2.5 pollution and associated health benefits in China during 2013–2017. *Sci. China Earth Sci.* **62**, 1847–1856 (2019).

4. Zhang, Q. et al. Drivers of improved $PM_{2.5}$ air quality in China from 2013 to 2017. *Proc. Natl Acad. Sci. USA* **116**, 24463–24469 (2019).
5. Li, K., Jacob, D. J., Shen, L., Lu, X., De Smedt, I. & Liao, H. Increases in surface ozone pollution in China from 2013 to 2019: anthropogenic and meteorological influences. *Atmos. Chem. Phys.* **20**, 11423–11433 (2020).
6. Liu, H. et al. Ground-level ozone pollution and its health impacts in China. *Atmos. Environ.* **173**, 223–230 (2018).
7. Lu, X. et al. Progress of air pollution control in China and its challenges and opportunities in the ecological civilization era. *Engineering* **6**, 1423–1431 (2020).
8. Zhou, H. et al. Distinguishing the impacts of natural and anthropogenic aerosols on global gross primary productivity through diffuse fertilization effect. *Atmos. Chem. Phys.* **22**, 693–709 (2022).
9. Unger, N., Zheng, Y., Yue, X. & Harper, K. L. Mitigation of ozone damage to the world's land ecosystems by source sector. *Nat. Clim. Change* **10**, 134–137 (2020).
10. Mercado, L. M. et al. Impact of changes in diffuse radiation on the global land carbon sink. *Nature* **458**, 1014–U1087 (2009).
11. Zhou, H. et al. Aerosol radiative and climatic effects on ecosystem productivity and evapotranspiration. *Curr. Opin. Environ. Sci. Health* **19**, 100218 (2021).
12. Zhang, Y. et al. Increased global land carbon sink due to aerosol-induced cooling. *Glob. Biogeochem. Cycles* **33**, 439–457 (2019).
13. Malavelle, F. F. et al. Studying the impact of biomass burning aerosol radiative and climate effects on the Amazon rainforest productivity with an Earth system model. *Atmos. Chem. Phys.* **19**, 1301–1326 (2019).
14. Keppel-Aleks, G. & Washenfelder, R. A. The effect of atmospheric sulfate reductions on diffuse radiation and photosynthesis in the United States during 1995-2013. *Geophys. Res. Lett.* **43**, 9984–9993 (2016).
15. Jing, X. et al. The effects of clouds and aerosols on net ecosystem CO_2 exchange over semi-arid Loess Plateau of northwest China. *Atmos. Chem. Phys.* **10**, 8205–8218 (2010).
16. Yue, X. & Unger, N. Fire air pollution reduces global terrestrial productivity. *Nat. Commun.* **9**, 5413 (2018).
17. Cohan, D. S., Xu, J., Greenwald, R., Bergin, M. H. & Chameides, W. L. Impact of atmospheric aerosol light scattering and absorption on terrestrial net primary productivity. *Glob. Biogeochem. Cycles* **16**, 1090 (2002).
18. Yue, X. et al. Ozone and haze pollution weakens net primary productivity in China. *Atmos. Chem. Phys.* **17**, 6073–6089 (2017).
19. Wittig, V. E., Ainsworth, E. A. & Long, S. P. To what extent do current and projected increases in surface ozone affect photosynthesis and stomatal conductance of trees? A meta-analytic review of the last 3 decades of experiments. *Plant Cell Environ.* **30**, 1150–1162 (2007).
20. Piao, S. et al. The carbon balance of terrestrial ecosystems in China. *Nature* **458**, 1009–1013 (2009).
21. Wang, J. et al. Large Chinese land carbon sink estimated from atmospheric carbon dioxide data. *Nature* **586**, 720–723 (2020).
22. Yue, X. et al. Development and evaluation of the interactive Model for Air Pollution and Land Ecosystems (iMAPLE) version 1.0. *Geosci Model Dev.* **17**, 4621–4642 (2024).
23. Sitch, S., Cox, P. M., Collins, W. J. & Huntingford, C. Indirect radiative forcing of climate change through ozone effects on the land-carbon sink. *Nature* **448**, 791–794 (2007).
24. Spitters, C. J. T., Toussaint, H. & Goudriaan, J. Separating the diffuse and direct component of global radiation and its implications for modeling canopy photosynthesis. Part 1. Components of incoming radiation. *Agric. For. Meteorol.* **38**, 217–229 (1986).
25. Yue, X. & Unger, N. Aerosol optical depth thresholds as a tool to assess diffuse radiation fertilization of the land carbon uptake in China. *Atmos. Chem. Phys.* **17**, 1329–1342 (2017).
26. Krishnamohan, K. S., Bala, G., Cao, L., Duan, L. & Caldeira, K. The climatic effects of hygroscopic growth of sulfate aerosols in the stratosphere. *Earth Future* **8**, e2019EF001326 (2020).
27. Li, K. et al. A two-pollutant strategy for improving ozone and particulate air quality in China. *Nat. Geosci.* **12**, 906–910 (2019).
28. Li, K. et al. Ozone pollution in the North China Plain spreading into the late-winter haze season. *Proc. Natl Acad. Sci. USA* **118**, e2015797118 (2021).
29. Yue, X. et al. Large potential of strengthening the land carbon sink in China through anthropogenic interventions. *Sci. Bull.* **69**, 2622–2631 (2024).
30. Yu, Z. et al. Forest expansion dominates China's land carbon sink since 1980. *Nat. Commun.* **13**, 5374 (2022).
31. Duan, J. et al. Absorbable aerosols based on OMI data: a case study in three provinces of Northeast China. *Environ. Monit. Assess.* **193**, 479 (2021).
32. Geng, G. et al. Tracking air pollution in China: near real-time $PM_{2.5}$ retrievals from multisource data fusion. *Environ. Sci. Technol.* **55**, 12106–12115 (2021).
33. Zhou, H. et al. Responses of gross primary productivity to diffuse radiation at global FLUXNET sites. *Atmos. Environ.* **244**, 117905 (2021).
34. Hong, S. et al. Divergent responses of soil organic carbon to afforestation. *Nat. Sustain.* **3**, 694–700 (2020).
35. Shi, S. & Han, P. Estimating the soil carbon sequestration potential of China's Grain for Green Project. *Glob. Biogeochem. Cycles* **28**, 1279–1294 (2014).
36. Xia, J. et al. Reconstructing long-term forest age of China by combining forest inventories, satellite-based forest age and forest cover data sets. *J. Geophys. Res. Biogeosci.* **128**, e2023JG007492 (2023).
37. Han, P. et al. Evaluating China's fossil-fuel CO_2 emissions from a comprehensive dataset of nine inventories. *Atmos. Chem. Phys.* **20**, 11371–11385 (2020).
38. Xinliang, X. *China's Multi-Year Provincial Administrative Division Boundary Data* (Resource and Environment Science and Data Center, Institute of Geographic Sciences and Natural Resources Research, Chinese Academy of Sciences, 2023); https://doi.org/10.12078/2023010103

Methods

Data-driven model

We used two machine learning algorithms, XGB and RF, to construct data-driven NPP models in combination with multi-source observations. As an updated gradient boosting machine algorithm, XGB can address overfitting problems in training datasets by applying regularized boosting and parallel processing[39]. XGB is trained using decision tree ensembles, including a set of classification and regression trees. The major calculation of XGB is as follows:

$$\hat{\mathbf{y}}_i = \sum_{k=1}^{k=N} f_k(x_i), \quad f \epsilon F \tag{1}$$

where $\hat{y}_i$ and x_i are the modelled output and initial input variables, N is the number of training trees, k represents a specific training tree, f is a function in the functional space F including the set of all possible classification and regression trees. The objective function to be optimized is then given using real values y_i as follows:

$$\text{obj}(\theta) = \sum_{i=1}^{N} l(y_i, \hat{\mathbf{y}}_i) + \sum_{k=1}^{k=N} \Omega(f_k) \tag{2}$$

where $l(y_i, \hat{\mathbf{y}}_i)$ and $\Omega(f_k)$ are the training loss function and regularization term. The training loss represents the performance of the predictive models with the training data. The regularization term controls the complexity of the predictive models, avoiding the overfitting problems.

RF is a widely recognized technique in machine learning with advanced efficacy in classification and regression tasks[40]. During the training process, the RF model constructs each decision tree using a randomly selected subset of the data along with a randomly selected subset of features for each split. This randomness not only introduces variability among individual trees, but also substantially reduces the risk of overfitting, thus enhancing the overall prediction accuracy. RF is particularly noted for its ability to manage complex datasets, reduce overfitting and yield reliable predictions compared with traditional methods. The fundamental computation involved in the RF model is shown as follows:

$$F(x) = \frac{1}{T}\sum_{t=1}^{T} f_t(x) \tag{3}$$

where $F(x)$ is the output, x is the input data, $f_t(x)$ is the model for each tree, and T is the number of total trees. The final output of the RF model is determined by averaging the predictions from each individual tree within the ensemble. This approach allows the RF model to leverage the strengths of multiple decision trees, mitigating the impact of errors in any single tree on the final prediction. Moreover, XGB and RF both use decision trees to construct predicted models in the training processes. Decision trees are often by nature immune to colinearity between input variables owing to the selection of the optimal feature[41]. For instance, when there are two input features of a decision tree model with intercorrelations of 99%, the decision tree model will choose only one of them as statistic feature during the process of deciding on a split.

Data-driven models have demonstrated superior performance compared with traditional methods in addressing complex environmental issues such as air pollution[42] and the terrestrial carbon cycle[43]. In this study, we applied both XGB and RF to construct predictive models for NPP in China using LCC, air pollutant and meteorology data as inputs. For LCC, we used the year-to-year forest and non-forest cover fraction developed by combining multiple satellite retrievals and the national forest inventory[36]. For air pollutants, we used monthly gridded concentrations of $PM_{2.5}$ and MDA8 O_3 from an assimilation data product combined with thousands of ground-based observation sites[32]. Given the spatial heterogeneity of CO_2, we used well-validated monthly gridded CO_2 datasets as inputs for the data-driven models. These datasets were derived from estimations that integrate a constrained ensemble Kalman filter in a carbon assimilation system that incorporates ground-based observations[44]. For meteorology, we used the 2 m temperature, shortwave radiation and precipitation from the fifth-generation reanalysis of global atmosphere dataset from the European Centre for Medium-Range Weather Forecasts (ERA-5)[45]. All input drivers were interpolated onto 0.5° × 0.5° grids and monthly timescales for 2013–2020 in China.

We developed XGB-NPP and RF-NPP models to assess the impacts of air pollutants on NPP in China. To construct the models, we randomly selected 80% of the total sample (291,152 data points) for training and reserved the remaining 20% (72,787 data points) for validation. The detailed parameters of both models are presented in Supplementary Table 1. We employed five- and tenfold cross-validations to evaluate the performance of the XGB-NPP and RF-NPP models during the training process. Specifically, the entire training dataset was randomly divided into five or ten folds, each containing an equal number of samples. For each iteration, four or nine folds were used to train models, while the remaining fold served as the test dataset to assess model performance. This process was repeated until each fold had been used as the test dataset. Our results showed that the XGB-NPP and RF-NPP models demonstrated high accuracy in estimating NPP, with $R^2 = 0.88$ (median values from fivefold cross-validation) and $R^2 = 0.89$ (median values of tenfold cross-validation) (Supplementary Table 2). These results confirm the excellent performance of data-driven models in avoiding overfitting and ensuring model robustness. Validations with all the derived datasets also demonstrated that both the XGB-NPP and RF-NPP models could accurately reproduce observed NPP in China from Global LAnd Surface Satellite data[46,47], exhibiting low biases of −0.34% and −0.23% and high correlations of 0.93 and 0.95, respectively (Supplementary Fig. 11).

We then performed two baseline experiments using year-to-year varied forcings (XGB_BASE or RF_BASE) to drive the developed machine learning models (Supplementary Table 3). To specifically examine the effects of air pollutant changes on NPP, we conducted two sensitivity experiments with fixed $PM_{2.5}$ and MDA8 O_3 concentrations set to the 2013 level (XGB_FIX_AIR or RF_FIX_AIR). The differences between BASE and FIX_AIR represented the NPP responses to changes in air pollutants. It is important to note that the XGB-NPP and RF-NPP models cannot isolate the impacts of the CAA plan on air pollution, because the changes in observed air pollutants result from both emissions controls and climatic variation. We also performed two sensitivity experiments to isolate the impacts of LCC on NPP, comparing simulations from XGB_BASE and RF_BASE and those using fixed LCC in 2013 (XGB_FIX_LCC and RF_FIX_LCC).

Process-based models

We used a suite of numerical models to explore the changes in air pollution and the associated ecological responses due to the CAA plan in 2014–2020. The GEOS-Chem (version 12-01) chemical transport model was used to predict CAA-induced changes in three-dimensional aerosol profiles and surface O_3 concentrations. GEOS-Chem simulates gas-phase pollutants and aerosols (sulfate, nitrate, BC, OC, dust and sea salt) based on a fully coupled NO_x–O_x–hydrocarbon–aerosol chemistry mechanism[48]. The model was driven with three-dimensional meteorological data from version 2 of NASA's Modern-Era Retrospective Analysis for Research and Applications (MERRA-2)[49] and two-dimensional surface anthropogenic and natural emissions. The anthropogenic emissions used in this study were adopted from the latest Multiresolution Emission Inventory in China (MEIC)[2]. In this study, GEOS-Chem simulated aerosol profiles and surface O_3 concentrations at a resolution of 0.5° × 0.625° over the whole of China. The outside boundary conditions were provided by global simulations at a horizontal resolution of 2° × 2.5° with year-to-year anthropogenic emissions from the Community Emissions Data System inventory.

The Column Radiative Model (CRM) was used to simulate AOD and the aerosol-induced changes in diffuse and direct surface radiation. As the standalone version of the radiative transfer module used by the National Center for Atmospheric Research (NCAR) Community Climate Model (http://www.cesm.ucar.edu/models/), the CRM calculates direct aerosol radiative effects (scattering and absorbing processes) with 20 vertical layers from the land surface to a height of 0.5 hPa at hourly intervals. The model calculates radiative perturbations by aerosols with optical parameters for sea salt[50] (coarse and accumulation modes), mineral dust[51] (clay and silt) and anthropogenic species[52] (sulfate, nitrate, BC and OC). Here the CRM was driven with hourly three-dimensional meteorological data from MERRA-2 reanalyses and 3 h cloud cover and liquid water path data from the Clouds and the Earth's Radiant Energy System SYN1deg product (http://ceres.larc.nasa.gov).

To assess aerosol climatic effects, we used the AOD–climate relationships derived from two Earth system models (ESMs): ModelE2 and CESM1 (Supplementary Section 2). For this study, we performed two simulations from 1990 to 2020 using ModelE2. In the first simulation, we applied year-to-year anthropogenic emissions from the Community Emissions Data System globally and from the MEIC for China. In the second simulation, we used the same configurations except that the MEIC emissions were fixed at 2013 levels for the period after 2013. Both simulations accounted for air–ocean coupling and direct and indirect aerosol radiative effects. The differences in AOD and climatic variables between the two runs represent the aerosol effects due to the control of anthropogenic emissions in China. For CESM1, we used the simulated changes in temperature and precipitation induced by domestic aerosol changes in China during 2013–2019 assessed in a recent study[53]. We collected the averages of AOD and climatic variables in China from both ESMs to derive climatic perturbations due to aerosol changes. These climatic sensitivities were applied in conjunction with simulated AOD changes from CRM to calculate CAA-induced changes in temperature (ΔTair) and precipitation (ΔPRE) as follows:

$$\Delta\mathrm{Tair}(i,j) = \Delta\mathrm{Tair}_{\mathrm{ESM}}(i,j) \times \frac{\Delta\mathrm{AOD}_{\mathrm{CRM}}}{\Delta\mathrm{AOD}_{\mathrm{ESM}}} \quad (4)$$

$$\Delta\mathrm{PRE}(i,j) = \Delta\mathrm{PRE}_{\mathrm{ESM}}(i,j) \times \frac{\Delta\mathrm{AOD}_{\mathrm{CRM}}}{\Delta\mathrm{AOD}_{\mathrm{ESM}}} \quad (5)$$

where $\Delta\mathrm{Tair}_{\mathrm{ESM}}(i,j)$ and $\Delta\mathrm{PRE}_{\mathrm{ESM}}(i,j)$ are the differences in Tair and PRE at each grid point (i,j) as simulated by ModelE2 or CESM1 with and without the anthropogenic emissions controls in China. $\frac{\Delta\mathrm{AOD}_{\mathrm{CRM}}}{\Delta\mathrm{AOD}_{\mathrm{ESM}}}$ is used to correct the biases in the simulated national average AOD changes caused by CAA plans for both models with mean AOD changes simulated by CRM (Supplementary Fig. 12). As a result, we performed two experiments using bias-corrected simulations from either ModelE2 or CESM1 to quantify the modelling uncertainties, and the ensemble mean of both ESMs was used to represent aerosol climatic effects.

iMAPLE[22] was used to simulate land carbon perturbations caused by aerosols and O_3. As the updated version of the Yale Interactive terrestrial Biosphere model[54], iMAPLE includes process-based carbon cycles, water cycles and their interactions. The model can dynamically simulate carbon fluxes, leaf area index, tree growth and the carbon allocation of nine plant functional types, as well as the prognostic soil temperature/moisture and evapotranspiration. Since 2020, iMAPLE (and the earlier version of the Yale Interactive terrestrial Biosphere model) has joined the multi-model ensemble project TRENDY to provide estimates of the global carbon budget[55]. Here iMAPLE was driven with hourly surface meteorological data from MERRA-2 reanalyses and annual LCC data from the latest land-cover data developed by combining national forest inventory, satellite-based forest age and forest cover datasets[36]. Leaf-level photosynthesis was calculated using the well-validated enzyme-kinetics[56] and stomatal conductance schemes[57]. The canopy was divided into sunlit and shaded leaves to distinguish the effects of direct and diffuse light, and plant photosynthesis was calculated as the sum of photosynthesis from sunlit and shaded leaves as follows:

$$A_{\mathrm{total}} = A_{\mathrm{sunlit}} \times F_{\mathrm{sunlit}} + A_{\mathrm{shaded}} \times (1 - F_{\mathrm{sunlit}}) \quad (6)$$

where A_{sunlit} and A_{shaded} are the photosynthesis of sunlit and shaded leaves, respectively. The fraction of the sunlit leaf area, F_{sunlit}, was calculated as follows:

$$F_{\mathrm{sunlit}} = \mathrm{e}^{-RL} \quad (7)$$

where L the is leaf area index at one canopy layer and R is the extinction coefficient defined as $0.5/\cos\alpha$ (α is the solar zenith).

The iMAPLE model calculates O_3 damage to plant photosynthesis using a well-established flux-based scheme[23]. The O_3 damage scheme assumes a reduced plant photosynthesis rate $F_{O_3,D}$ as a function of the stomatal O_3 flux F_{O_3}:

$$F_{O_3,D} = \begin{cases} -f_{O_3} \times (F_{O_3} - T_{O_3}), & \text{if } F_{O_3} > T_{O_3} \\ 0, & \text{if } F_{O_3} \le T_{O_3} \end{cases} \quad (8)$$

where f_{O3} is the O_3 sensitivity coefficient and T_{O_3} is the damage threshold. F_{O_3} is dependent on the ambient O_3 concentration and stomatal conductance (g_s). f varies, with low to high values for each plant functional type to represent the uncertainties in O_3 sensitivity corresponding to each species[23]. T_{O_3} indicates the plant tolerance to O_3 concentrations, and $F_{O_3,D}$ is negative when F_{O_3} is higher than T_{O_3}.

Simulations

We performed 2 GEOS-Chem runs, 17 CRM runs and 34 iMAPLE runs to isolate the impacts of O_3 and aerosols on NPP in China following the implementation of the CAA plan (Supplementary Table 4). The GEOS-Chem runs, GC_BASE and GC_FIX, were driven with the same meteorological conditions and natural emissions, but in the GC_BASE run we used the year-to-year anthropogenic emissions following the implementation of the CAA plan, while in the GC_FIX run we used anthropogenic emissions fixed at 2013 levels without the implementation of the CAA plan. The differences between GC_BASE and GC_FIX represented the O_3 and aerosol concentration changes resulting from the CAA plan without meteorological influences, following the methods used by Zhang et al.[4]. Both experiments provided three-dimensional concentrations of different aerosol types, including sulfate, nitrate, OC, BC, dust and sea salt, for use in CRM.

The CRM runs included the CRM_NA run without aerosol effects, the CRM_BASE run with aerosol profiles from GC_BASE and the CRM_FIX run with aerosol profiles from GC_FIX. The impacts of individual aerosol species on surface photosynthetically active radiation (PAR) were isolated with specific aerosol profiles derived from either GC_BASE or GC_FIX. For example, the BC outputs from the GC_BASE model run were used to drive the CRM (CRM_BC) to quantify surface radiative perturbations by BC aerosols. For aerosol climatic effects, we used AOD differences between CRM_BASE and CRM_FIX/CRM_NA experiments along with the climatic sensitivity from two ESMs. These data were utilized to calculate the responses of temperature and precipitation to aerosol changes following equations (4) and (5).

Both the radiative effects (simulated changes in surface diffuse and direct PAR from CRM) and climatic effects (simulated changes in meteorological variables based on ESM sensitivity and AOD from CRM) of aerosols were used to drive the iMAPLE model to explore the NPP changes caused by aerosol perturbations. For the O_3 damage effect, four iMAPLE runs, IM_BOH (IM_BOL) and IM_FOH (IM_FOL), were performed using the O_3 concentrations output from the GC_BASE and GC_FIX model runs with high (low) O_3 damage sensitivities. We also performed an extra experiment to isolate LCC impacts on national

NPP in China using the difference in simulations between variable (IM_BASE) and fixed LCC (IM_LCC). All simulations were performed for the 2013–2020 period with a 200 yr spin-up period for vegetation and soil carbon pools. Surface O_3 simulated at a 0.5° × 0.625° resolution from GEOS-Chem and the radiative fluxes at a 1° × 1° resolution from CRM were downscaled to a resolution of 0.25° × 0.3125° for use in iMAPLE to calculate the NPP responses to aerosols and O_3 changes caused by the CAA plan.

Model validations

The O_3 concentrations simulated with GEOS-Chem showed a spatial pattern that was similar to the ground-based observations (with correlations of 0.82) but overestimated the concentrations by up to 15.2% during 2014–2015 (Fig. 1). This overestimation may have been related to the large sample of urban sites in the observational network. An earlier study[58] found a moderate bias of 4% in the surface O_3 simulated with GEOS-Chem compared with that measured at 115 sites in China from the same network that excluded urban sites. The biases in simulated O_3 might therefore have had limited impacts on the NPP results in this study because high vegetation coverage occurs mainly in rural areas. The AOD simulations obtained with CRM effectively reproduced the satellite-observed spatial pattern with correlations of 0.91 and annual trends (Fig. 1). Regionally, the simulations slightly overestimated the AOD over the SCB and NCP with high anthropogenic emissions, but underestimated the AOD over northwest China owing to fewer dust aerosols in this region (Supplementary Fig. 13). The simulated AOD showed decreasing trends over most areas, consistent with previous studies that incorporated ground-based observations[59]. Regarding aerosol species, we found that the simulated BC AOD matched the satellite-retrieved AODs with regards to both the spatial distribution and temporal variations in eastern China (Supplementary Fig. 7).

iMAPLE reproduced the observed spatial carbon flux pattern with high correlation coefficients of 0.89 ($P < 0.01$) for gross primary productivity (GPP) and 0.75 ($P < 0.01$) for NPP compared with the satellite-based products (Supplementary Fig. 14). The comparisons also yielded small biases of −7.78% for GPP and 15.17% for NPP. Meanwhile, the simulated mean and trends in leaf area index also presented similar spatiotemporal variations of 1.05 and 0.01 yr^{-1} with satellite-based observations of 1.03 and 0.01 yr^{-1} (Supplementary Fig. 15). Furthermore, iMAPLE predicted reasonable GPP responses to O_3 and diffuse radiation. To explore the diffuse effects, we performed site-level simulations at 167 FLUXNET sites providing long-term hourly diffuse radiation data[33]. We separated solar radiation into diffuse (diffuse fraction > 0.8) and direct (diffuse fraction < 0.2) conditions following the methods described by Mercado et al.[10] (Supplementary Fig. 8). The observations and simulations both showed that GPP grew faster under more diffuse conditions. The diffuse fertilization efficiency, defined as the percentage change in GPP per unit of diffuse radiation, was 0.15–1.06% W^{-1} m^2 from the observations and 0.11–1.09% W^{-1} m^2 from simulations. For sites in China, the simulated diffuse fertilization efficiency of 0.11–0.84% W^{-1} m^2 was also close to the observed diffuse fertilization efficiency of 0.32–0.92% W^{-1} m^2 (Supplementary Fig. 9). Regarding the O_3 damage effects, iMAPLE simulated reasonable damage effects compared with global observations from hundreds of published studies with different plant functional types[16].

We also evaluated the performance of the CRM in simulating shortwave radiation and the diffuse fraction in China. The simulations showed a similar spatial pattern to the Clouds and the Earth's Radiant Energy System observations, with high correlation coefficients of 0.94 ($P < 0.01$) and 0.92 ($P < 0.01$) and low biases of 3.7% and −13.6% for shortwave radiation and the diffuse fraction, respectively (Supplementary Fig. 16). Large diffuse fraction underestimations were found mainly over northwest China, which has very low vegetation coverage. The comparisons showed a bias of −4.8% for the diffuse fraction over eastern China with high GPP and NPP. Based on the CRM outputs, our simulations showed that aerosols reduced direct solar radiation by 16.3 W m^{-2} nationwide and 23 W m^{-2} in the eastern region for 2013–2020, weaker than previous estimates of −21.9 W m^{-2} over all of China[60] and −28 W m^{-2} in the eastern part[61]; these differences are probably due to the higher aerosol loading before 2010 considered in the latter studies. Furthermore, compared with satellite-based data products and simulations from other radiative models, CRM reproduced reasonable direct aerosol radiative effects in China with regards to both the spatial pattern and magnitude[25].

Data availability

All simulations that support the finding of this study and source data underlying Figs. 1–5 are publicly available via Figshare at https://doi.org/10.6084/m9.figshare.27186126.v1 (ref. 62). The data used in this study are available publicly from the following databases. GLASS 8-day 500 m NPP and leaf area index data were obtained from the University of Maryland at http://www.glass.umd.edu/. The land-cover data in China are available via the National Ecosystem Research Network Data Center at https://doi.org/10.12199/nesdc.ecodb.rs.2023.015 (ref. 63). Gridded $PM_{2.5}$ and MDA8 O_3 data were downloaded from Tsinghua University at http://tapdata.org.cn. The meteorological datasets are from the ERA-5 reanalysis (https://www.ecmwf.int/) and monthly spatial CO_2 data are available in ref. 44.

Code availability

The codes for the processed-based and data-driven models are publicly available from the following sources. The codes for iMAPLE are available via Figshare at https://doi.org/10.6084/m9.figshare.23593578.v1 (ref. 64) and CRM is openly available at https://www.ess.uci.edu/~zender/. GEOS-Chem is developed and updated by the Atmospheric Chemistry Modeling Group at Harvard University and is available at https://acmg.seas.harvard.edu/geos/. The Python codes for XGB and RF used in the data-driven models are available at https://xgboost.readthedocs.io/en/latest/python/ and https://scikit-learn.org/stable/modules/ensemble.html, respectively.

References

39. Zhang, W. et al. State-of-the-art review of soft computing applications in underground excavations. *Geosci. Front.* **11**, 1095–1106 (2020).
40. Chen, J. et al. A comparison of linear regression, regularization, and machine learning algorithms to develop Europe-wide spatial models of fine particles and nitrogen dioxide. *Environ. Int.* **130**, 104934 (2019).
41. Zhou, H. et al. Distinguishing the main climatic drivers to the variability of gross primary productivity at global FLUXNET sites. *Environ. Res. Lett.* **18**, 124007 (2023).
42. Park, S. et al. Robust spatiotemporal estimation of PM concentrations using boosting-based ensemble models. *Sustainability* **13**, 13782 (2021).
43. Wang, H. et al. Exploring complex water stress–gross primary production relationships: impact of climatic drivers, main effects, and interactive effects. *Glob. Change Biol.* **28**, 4110–4123 (2022).
44. Liu, Z. et al. Improving the joint estimation of CO_2 and surface carbon fluxes using a constrained ensemble Kalman filter in COLA (v1.0). *Geosci. Model Dev.* **15**, 5511–5528 (2022).
45. Muñoz-Sabater, J. et al. ERA5-Land: a state-of-the-art global reanalysis dataset for land applications. *Earth Syst. Sci. Data* **13**, 4349–4383 (2021).
46. Liang, S. et al. A long-term Global LAnd Surface Satellite (GLASS) data-set for environmental studies. *Int. J. Digit. Earth* **6**, 5–33 (2013).
47. Liang, S. et al. The Global Land Surface Satellite (GLASS) product suite. *Bull. Am. Meteorol. Soc.* **102**, E323–E337 (2021).

48. Bey, I. et al. Global modeling of tropospheric chemistry with assimilated meteorology: model description and evaluation. *J. Geophys. Res. Atmos.* **106**, 23073–23095 (2001).
49. Gelaro, R. et al. The Modern-Era Retrospective analysis for Research and Applications, version 2 (MERRA-2). *J. Clim.* **30**, 5419–5454 (2017).
50. Yue, X. & Liao, H. Climatic responses to the shortwave and longwave direct radiative effects of sea salt aerosol in present day and the last glacial maximum. *Clim. Dynam.* **39**, 3019–3040 (2012).
51. Yue, X., Wang, H. J., Liao, H. & Fan, K. Simulation of dust aerosol radiative feedback using the GMOD: 2. Dust-climate interactions. *J. Geophys. Res. Atmos.* **115**, 843–858 (2010).
52. Giorgi, F. et al. RegCM4: model description and preliminary tests over multiple CORDEX domains. *Clim. Res.* **52**, 7–29 (2012).
53. Gao, J. et al. Climate responses in China to domestic and foreign aerosol changes due to clean air actions during 2013–2019. *npj Clim. Atmos. Sci.* **6**, 160 (2023).
54. Yue, X. & Unger, N. The Yale Interactive terrestrial Biosphere model version 1.0: description, evaluation and implementation into NASA GISS ModelE2. *Geosci. Model Dev.* **8**, 2399–2417 (2015).
55. Friedlingstein, P. et al. Global carbon budget 2020. *Earth Syst. Sci. Data* **12**, 3269–3340 (2020).
56. Farquhar, G. D., Caemmerer, S. V. & Berry, J. A. A biochemical-model of photosynthetic CO_2 assimilation in leaves of C_3 species. *Planta* **149**, 78–90 (1980).
57. Ball, J. T., Woodrow, I. E. & Berry, J. A. in *Progress in Photosynthesis Research* Vol. 4 (ed. Biggins, J.) 221–224 (Springer, 1987).
58. Sun, L. et al. Impacts of meteorology and emissions on summertime surface ozone increases over central eastern China between 2003 and 2015. *Atmos. Chem. Phys.* **19**, 1455–1469 (2019).
59. Li, J., Jiang, Y. W., Xia, X. G. & Hu, Y. Y. Increase of surface solar irradiance across east China related to changes in aerosol properties during the past decade. *Environ. Res. Lett.* **13**, 034006 (2018).
60. Chen, L., Shi G., Wang, B. & Zhang, P. Assessment on aerosol direct radiative forcing over China land areas based on satellite data. In *Proc. Remote sensing of the environment: the 17th China Conference on Remote Sensing* 82031A (SPIE, 2011).
61. Folini, D. & Wild, M. The effect of aerosols and sea surface temperature on China's climate in the late twentieth century from ensembles of global climate simulations. *J. Geophys. Res. Atmos.* **120**, 2261–2279 (2015).
62. Zhou, H. et al. Recovery of ecosystem productivity in China by the Clean Air Action plan. *figshare* https://doi.org/10.6084/m9.figshare.27186126.v1 (2024).
63. Tian, C. Interactive Model for Air Pollution and Land Ecosystems (iMAPLE) version 1.0. *figshare* https://doi.org/10.6084/m9.figshare.23593578.v1 (2023).
64. Xia, X. et al. *Land Use, Coverage and Change Dataset in China from 1980 to 2021* (National Ecological Data Center, 2023); https://doi.org/10.12199/nesdc.ecodb.rs.2023.015

Acknowledgements

This work was jointly supported by the National Natural Science Foundation of China (grant numbers 42293323 and 42275128 to X.Y.), the Natural Science Foundation of Jiangsu Province (grant number BK20220031 to X.Y.) and the National University of Defense Technology Independent Research Project (grant number ZK24-52 to H.Z.).

Author contributions

H.Z., X.Y. and H.L. conceived this project. X.Y. led the research and was responsible for communicating with all authors about the data, methods and results. H.Z. collected observational data and performed simulations with input from H.D., G.G. and W.Y. H.Z. completed data analyses and the first draft of the paper. X.Y. and H.L. reviewed and edited the paper. J.C., G.S., T.Z. and J.Z. helped to revise the paper.

Competing interests

The authors declare no competing interests.

Additional information

Extended data is available for this paper at https://doi.org/10.1038/s41561-024-01586-z.

Supplementary information The online version contains supplementary material available at https://doi.org/10.1038/s41561-024-01586-z.

Correspondence and requests for materials should be addressed to Xu Yue.

Peer review information *Nature Geoscience* thanks Xitian Cai, William Collins and the other, anonymous, reviewer(s) for their contribution to the peer review of this work. Primary Handling Editor: Xujia Jiang, in collaboration with the *Nature Geoscience* team.

https://doi.org/10.1038/s41561-024-01586-z

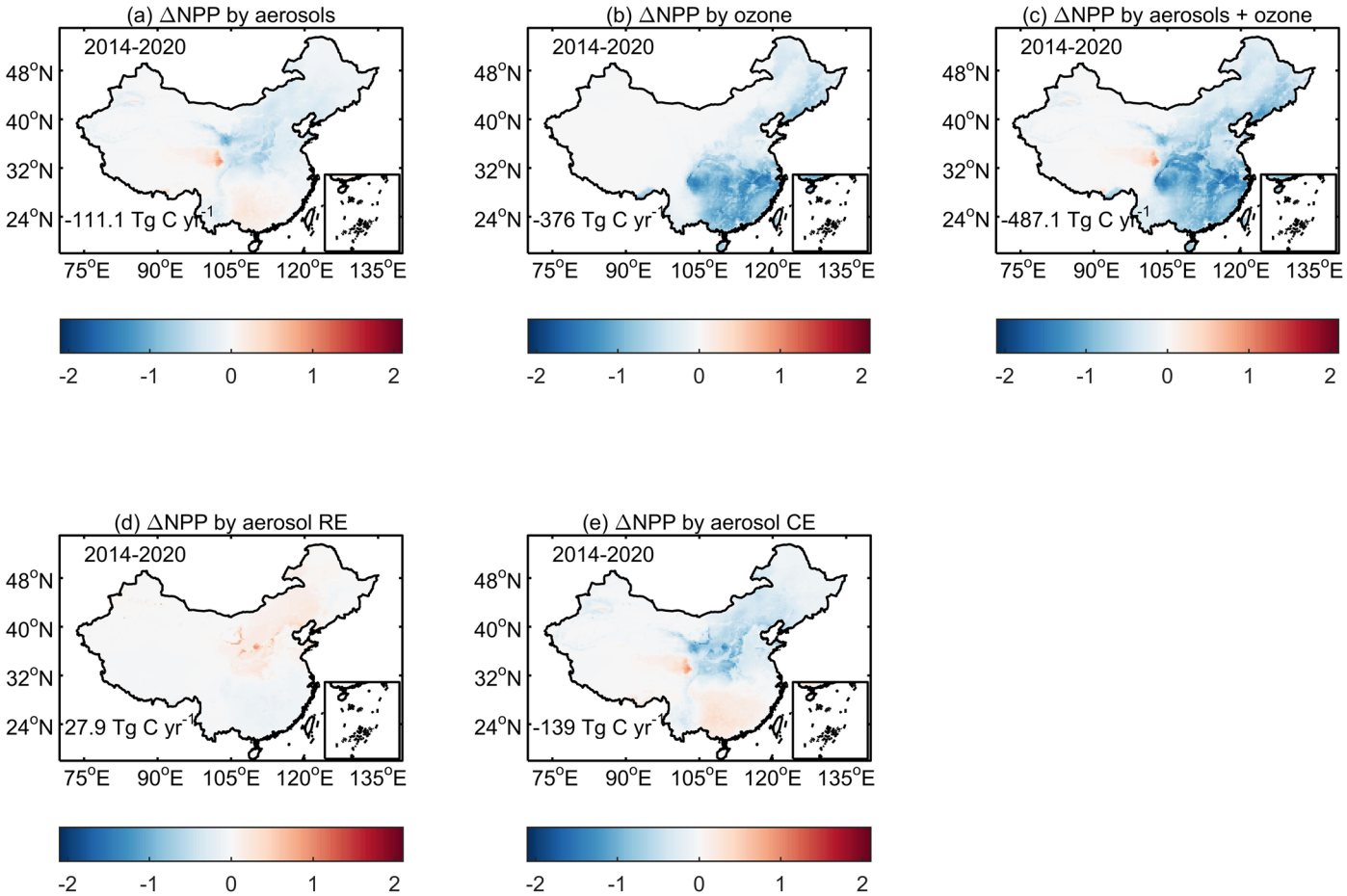

Extended Data Fig. 1 | Spatial pattern of NPP changes due to baseline air pollutants. Results shown are the changes of NPP (g C m^{-2} day^{-1}) during May-September caused by (**a**) aerosols, (**b**) ozone, and (**c**) their combined effects during 2014-2020 from simulations with and without air pollutants. The aerosol impacts are further separated into (**d**) radiative and (**e**) climatic effects on NPP. The national total changes in NPP (Tg C yr^{-1}) are shown on each panel. Basemaps (including inset maps) of China are adopted from the Resource and Environment Science and Data Center, ref. 38.

https://doi.org/10.1038/s41561-024-01586-z

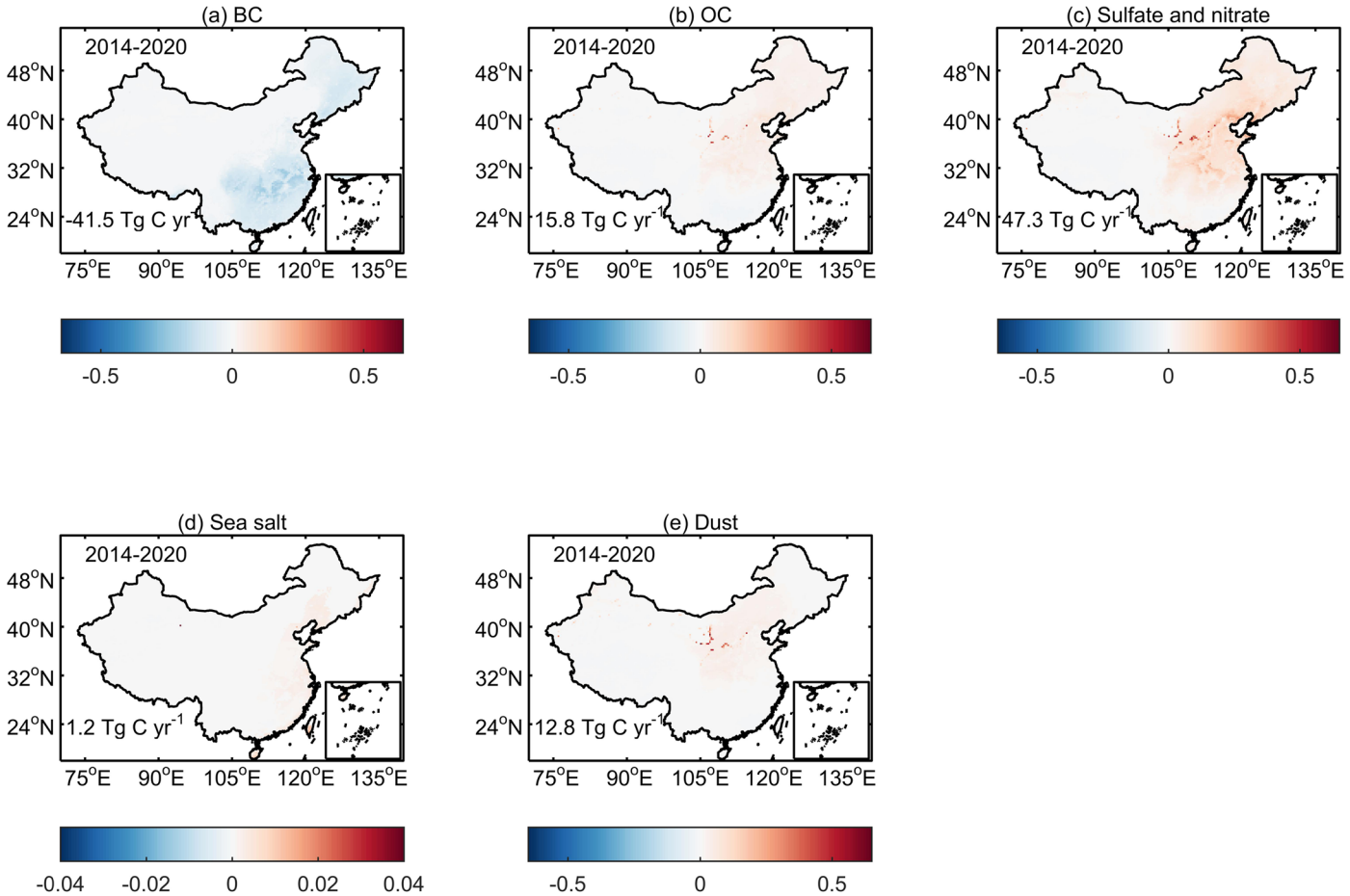

Extended Data Fig. 2 | Responses of NPP to the radiative effects of baseline aerosol species. Results shown are the impacts of five aerosol species including (**a**) black carbon, (**b**) organic carbon, (**c**) sulfate and nitrate, (**d**) sea salt and (**e**) dust on May-September NPP in China during 2014-2020 through perturbations in diffuse and direct radiation. Please notice the differences in color scales. The units are g C m^{-2} day^{-1}. Basemaps (including inset maps) of China are adopted from the Resource and Environment Science and Data Center, ref. 38.

https://doi.org/10.1038/s41561-024-01586-z

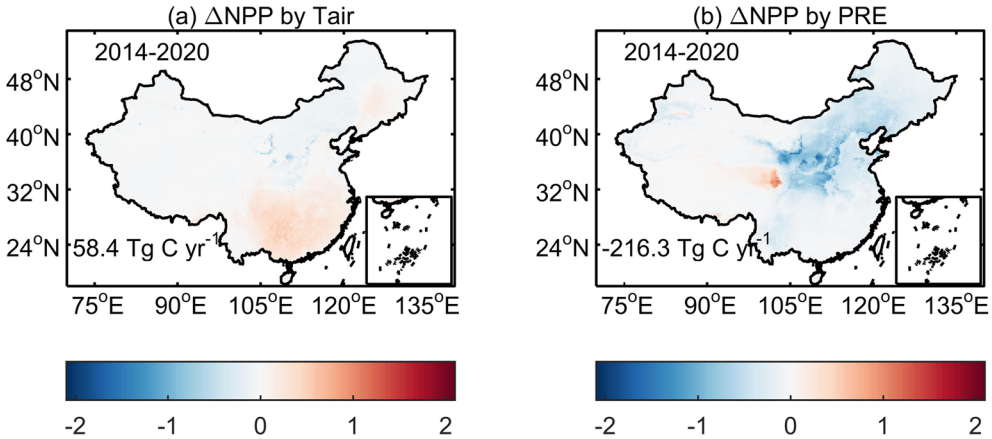

Extended Data Fig. 3 | Responses of NPP to baseline aerosol climatic effects. Results shown are the impacts of aerosol-induced changes in (**a**) temperature and (**b**) precipitation on May-September NPP (g C m^{-2} day^{-1}) in China during 2014-2020. Basemaps (including inset maps) of China are adopted from the Resource and Environment Science and Data Center, ref. 38.

https://doi.org/10.1038/s41561-024-01586-z

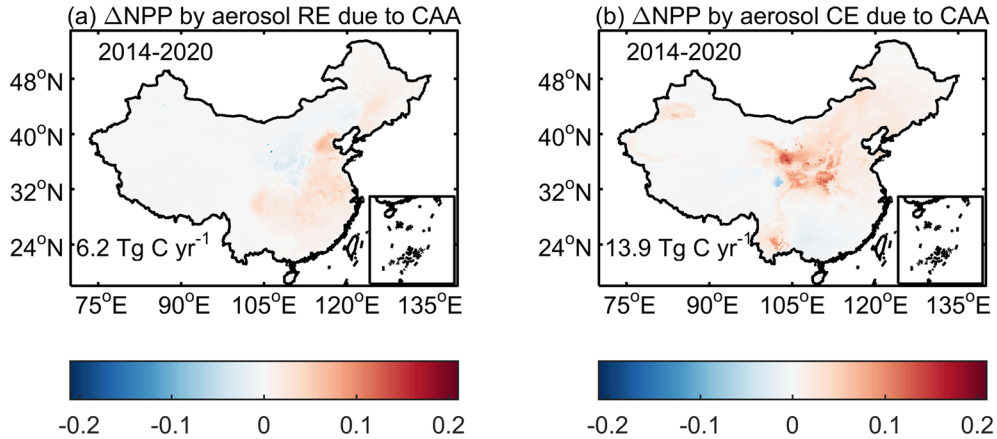

Extended Data Fig. 4 | NPP recovery due to changes in aerosol radiative and climatic effects following CAA plans in China. Results shown are the changes in May-September NPP (g C m^{-2} day^{-1}) due to the CAA-induced changes in aerosol (**a**) radiative and (**b**) climatic effects during 2014-2020. Basemaps (including inset maps) of China are adopted from the Resource and Environment Science and Data Center, ref. 38.

https://doi.org/10.1038/s41561-024-01586-z

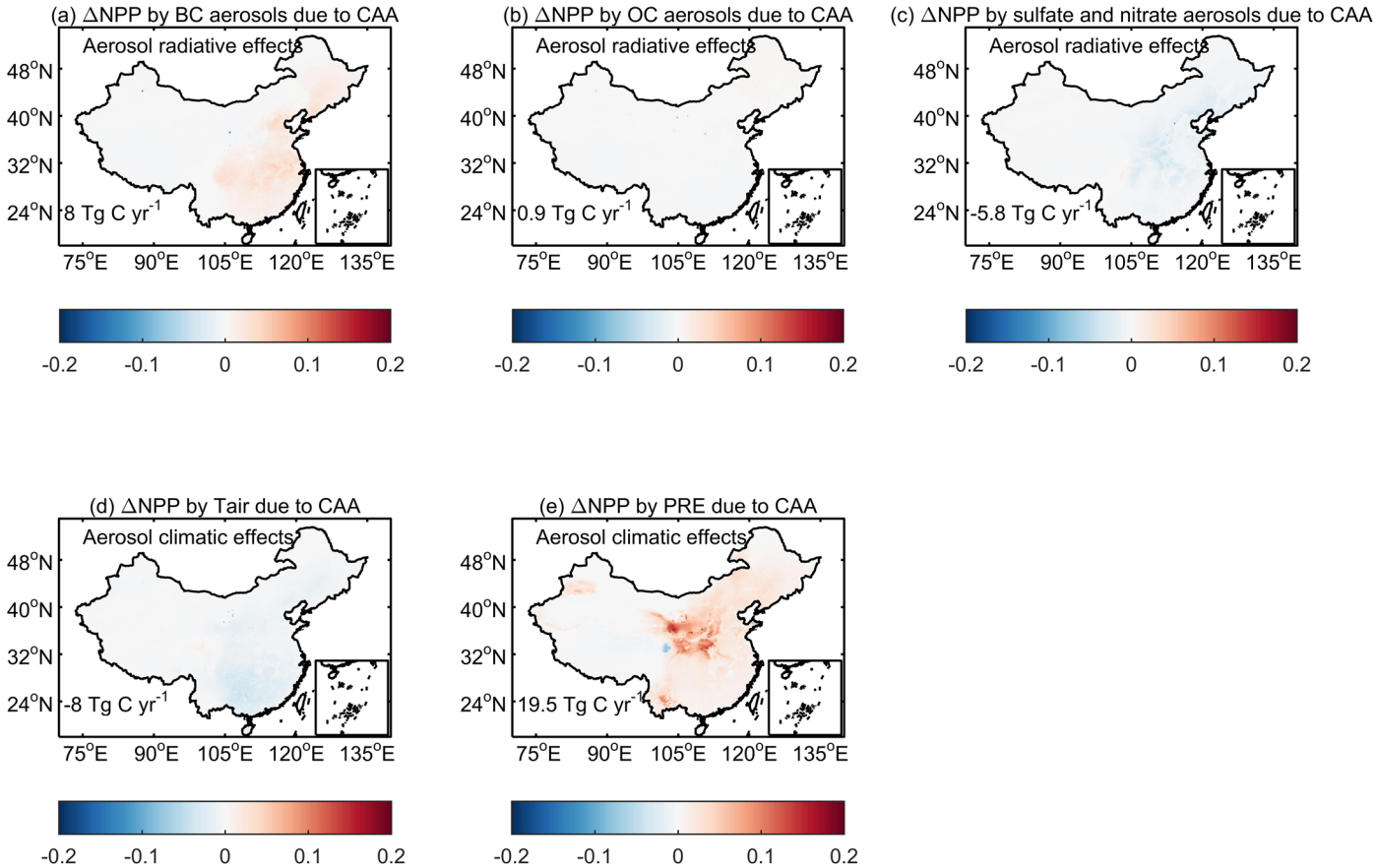

Extended Data Fig. 5 | NPP responses to changes in aerosol radiative and climatic effects following CAA plans in China. Results shown are the changes in May-September NPP (g C m^{-2} day^{-1}) due to the CAA-induced changes in aerosol radiative effects from (**a**) BC, (**b**) OC, and (**c**) sulfate and nitrate, as well as those of aerosol climatic effects from perturbations in (**d**) temperature and (**e**) precipitation. Basemaps (including inset maps) of China are adopted from the Resource and Environment Science and Data Center, ref. 38.